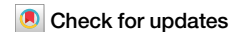
A Nature Portfolio journal



https://doi.org/10.1038/s43247-025-02515-7

The state and fate of Glaciar Perito Moreno Patagonia



Moritz Koch ® ¹ ⊠, Christian Sommer ® ¹, Norbert Blindow¹, Katrina Lutz¹, Pedro Skvarca², Lucas Ruiz ® ³, Paola Rizzoli⁴, Jose-Luis Bueso-Bello⁴, Johannes J. Fürst ® ¹ & Matthias H. Braun ® ¹

Glaciar Perito Moreno, located in the Southern Patagonian Icefields, has long been considered stable despite widespread regional glacier retreat. Unlike neighboring glaciers, its frontal position and surface elevation remained relatively unchanged - until recently. For lake-terminating glaciers, retreat is strongly controlled by their basal topography, which remains poorly known for Glaciar Perito Moreno. Here, we present helicopter-borne ground-penetrating radar and bathymetric data, along with time series of surface elevation and velocity. We detect an acceleration in frontal surface lowering rates, from 0.34 m a⁻¹ (2000–2019) to 5.5 m a⁻¹ (2019–2024), accompanied by glacier acceleration and retreat. Using a simple numerical model projecting current thinning into the future, we demonstrate the potential for large scale buoyancy-driven retreat once the glacier recedes beyond a subglacial ridge. These findings reveal a high sensitivity to frontal dynamics and suggest that Glaciar Perito Moreno may now be following a similar pattern of other retreating lacustrine calving glaciers in Patagonia.

The Patagonian ice masses experience some of the highest mass loss rates on the globe¹⁻³. The two largest icefields in Patagonia, the Northern Patagonian Icefield and the Southern Patagonian Icefield (SPI) are the main contributors to sea-level rise from South America⁴. The region is characterized by extreme accumulation and frontal ablation rates of large outlet glaciers⁵. Since 2000, these large water- terminating glaciers have accounted for most of the mass loss, with increasing rates driven by frontal ablation^{6,7}. These mass losses are primarily attributed to large glaciers undergoing rapid retreat accompanied by high velocity changes near their frontal positions^{8–10}. In the period from 2000 to 2019, the SPI recorded a mass loss rate of around -21 ± 1.7 Gt a⁻¹ due to frontal ablation of lake and ocean terminating glaciers¹⁰. However, glacier retreat across the SPI is characterized by high spatial and temporal heterogeneity^{9,11}. For instance, Glaciar Upsala (see Fig. 1a) contributed to the aforementioned mass loss at a rate of -1.4 ± 0.4 Gt a⁻¹, primarily during a large-scale retreat from 2008 to 2010. Glaciar O'Higgins, on the other hand, exhibited a loss of -1.7 ± 0.4 Gt a⁻¹ between 2010 and 2019, following a relatively stable frontal position for the preceding 15 years 10,12,13.

Declared a World Heritage Site by UNESCO in 1981, Glaciar Perito Moreno has become a tourist attraction due to its famous calving and lake-damming events and the infrastructure built around it. In 2023, almost 800,000 (663,674 in 2022) tickets were sold to Parque Nacional Los Glaciares, which is the entry point to the Glaciar Perito Moreno 14. Throughout the year, almost 90% of all visitors arriving in El Calafate, the

national park gateway, eventually visit the Glaciar Perito Moreno, making the glacier an important driver of the local economy^{14,15}. In the past, various studies have described Glaciar Perito Moreno as being relatively stable compared to other large outlet glaciers in Patagonia^{8–10,16,1} ⁷. From 1999 to 2013, the ice front position fluctuated by no more than 50 m, and during this period, surface velocity exhibited a seasonal variation of approximately 15% between the summer and winter month¹⁸. In general, the climate sensitivity of a glacier refers to its response to climatic variables such as temperature and precipitation¹⁹. Variability in precipitation has been identified as the primary driver of interannual variations in mass balance, while temperature fluctuations play a comparatively minor role. However, accumulation rates remain a substantial source of uncertainty²⁰. Air temperature records measured near the glacier terminus from the mid-1990s to 2020 indicate a decadal warming trend of 0.2° ± 0.1 °C. During this period, particularly strong warming was observed in summer (0.31° ± 0.1 °C in DJF) and spring (0.27° ± 0.2 °C in SON), contributing to increased surface melt⁵. During positive Southern Annular Mode phases and La Niña events, enhanced westerly winds lead to higher temperatures and stronger winds, which subsequently lead to a decrease in the glacier's surface mass balance⁵. Contrary to land-terminating glaciers, glacier response of a calving glacier is also strongly controlled by the bedrock setting near the glacier terminus 12,21,22. For example, topographic pinning points play an important role in glacier stability, and can prevent or delay its retreat^{21,23}.

¹Institut für Geographie, Friedrich-Alexander-Universität Erlangen-Nürnberg, Erlangen, Germany. ²Glaciarium - Glacier Interpretive Center, El Calafate, Argentina. ³Instituto Argentino de Nivología, Glaciología y Ciencias Ambientales, CONICET. UnCuyo, Gob. de Mendoza, Mendoza, Argentina. ⁴DLR, Microwaves and Radar Institute, Weßling, Germany. — e-mail: moritz.koch@fau.de

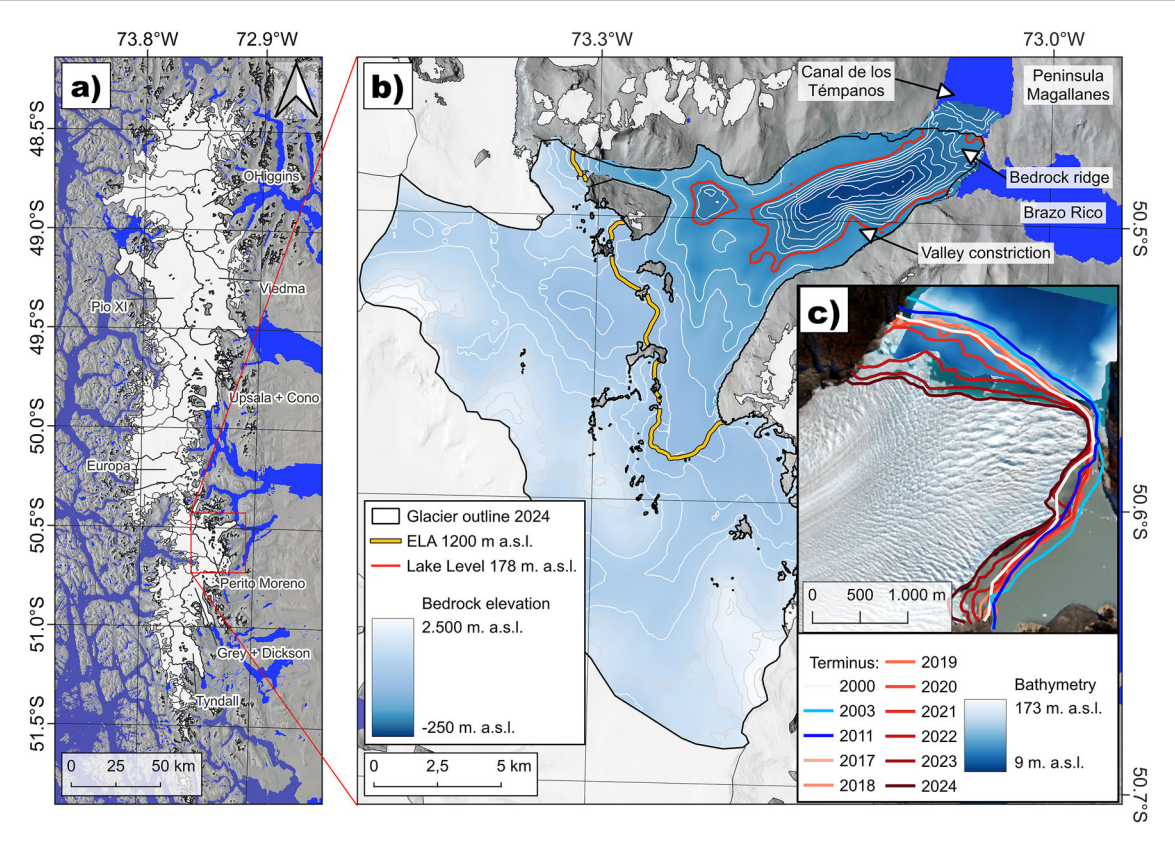


Fig. 1 | The Southern Patagonian Icefield and the location of Glaciar Perito Moreno, its bedrock topography and frontal change. a Overview of the Southern Patagonian Icefield (white). Background: SRTM hillshade and SRTM water body mask. Solid black lines are the outlines of the glaciers according to the Randolph Glacier Inventory (v7.0). The red square indicates the location of Glaciar Perito Moreno. b The bedrock topography of Glaciar Perito Moreno and Canal de los Témpanos. Contour lines below the lake level (solid red) have a 50 m spacing, above

it 200 m contours are used. The orange line indicates the ELA at 1200 m a.s.l. The solid black line indicates the glacier outline of 2024. Grey base map is a hill shaded SRTM digital elevation model. c Sentinel-2 optical image of the terminal position in May 2023. The white to red lines indicate the terminal position in April of each year delineated from Sentinel-2 and Landsat-7 imagery with the exception of 2003 and 2011 where November scenes were used.

Glacier fronts have been observed to remain at pinning points for extended periods following shifts in climatic conditions²⁴.

Prior to this study, the bedrock configuration of Glaciar Perito Moreno, particularly in the ablation zone, was largely unknown. Only seismic measurements along two profiles were carried out on the central tongue of the glacier in 1996²⁰ and a single borehole, drilled in 2010 ~5 km from the terminus²⁵. Accurate knowledge of glacier geometry is essential for predicting glacier evolution using models. In this context, geometry refers to both the glacier surface and the underlying bed topography. Although the surface can be observed directly, for example via satellite remote sensing, the retrieval of the bed topography is a more challenging process. Generally, the bed topography is derived by reconstructing the ice thickness and subtracting it from the surface elevation²⁶. The use of helicopter-borne Ground Penetrating Radar (GPR) is the most viable method of accurately assessing large areas of highly crevassed glaciers in steep mountainous terrain. Having information about the ice thickness distribution at a given time can then subsequently serve as an input for modelling approaches that reconstruct the ice thickness distribution of entire glacier catchments^{26–32}.

The aim of this study is to systematically quantify the current state and future fate of Glaciar Perito Moreno. On March 19 and 23, 2022, we conducted an ice thickness survey of the glacier using a helicopter-borne 25 MHz ground-penetrating radar system. Additionally, the proglacial lake bed in the Canal de los Témpanos (Fig. 1b), near the ice front, was bathymetrically surveyed on March 30, 2023. These measurements were incorporated into an established ice thickness reconstruction method to derive the bedrock topography of the entire glacier domain³¹. We analyzed surface elevation changes from 2000 to 2024 based on NASA's Shuttle Radar Topography Mission (SRTM) and repeat acquisitions of the TerraSAR-X

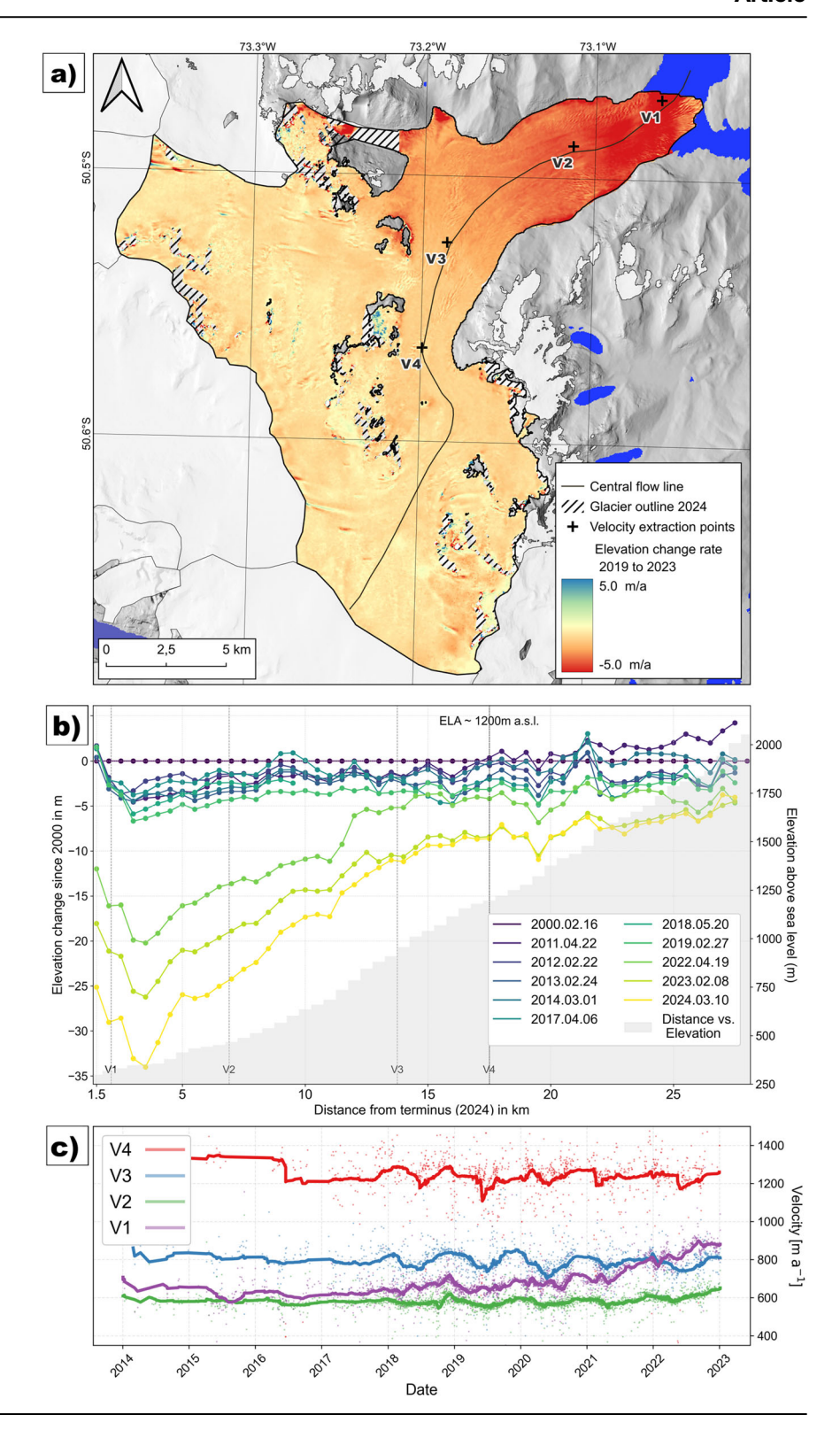
add-on for Digital Elevation Measurement Mission (TanDEM-X). Surface velocity profiles were derived from NASA's Inter-Mission Time Series of Land Ice Velocity and Elevation (ITS_Live) datasets^{33–35}. A conceptual model was developed to project the potential future evolution of the glacier based on buoyancy-driven retreat. Using our acquired bedrock topography data along with time series of glacier surface and ice velocity, we aim to provide insights into the glacier's past stability, current ice dynamics, and future trajectory.

Results

The fate of Glaciar Perito Moreno

Glaciar Perito Moreno (50.5°S, 73.2°W) is located on the eastern, Argentinian side of the Southern Patagonian Icefield (Fig. 1a). It covers an area of 259 km² (2007) ranging from 190 m a.s.l. to 2850 m a.s.l. flowing eastwards. The terminus calves into the junction of the northern Canal de los Témpanos and the eastern Brazo Rico of Lago Argentino, separated by Península Magallanes, where the glacier has dammed the lake many times in the past²⁰. Figure 1b shows the bedrock topography of Glaciar Perito Moreno. The reconstruction of ice thickness, incorporating recently acquired GPR (see Supplementary Fig. S7) data, yields notable findings. At the glacier front, a subglacial ridge is unveiled, which is a continuation of the Península Magallanes. The contour lines in the central part of the terminus show the position of the bedrock ridge extending from Península Magellanes, dividing the ice flow to the north and east. As shown in Fig. 1c, the presence of the ridgeline is also reflected in the surface morphology and orientation of the crevasses in the optic satellite imagery. A greater portion of the main glacier trunk flows into the northern terminus via a deep glacial trough. The trough is deeper towards the northern shoreline of the Canal de los

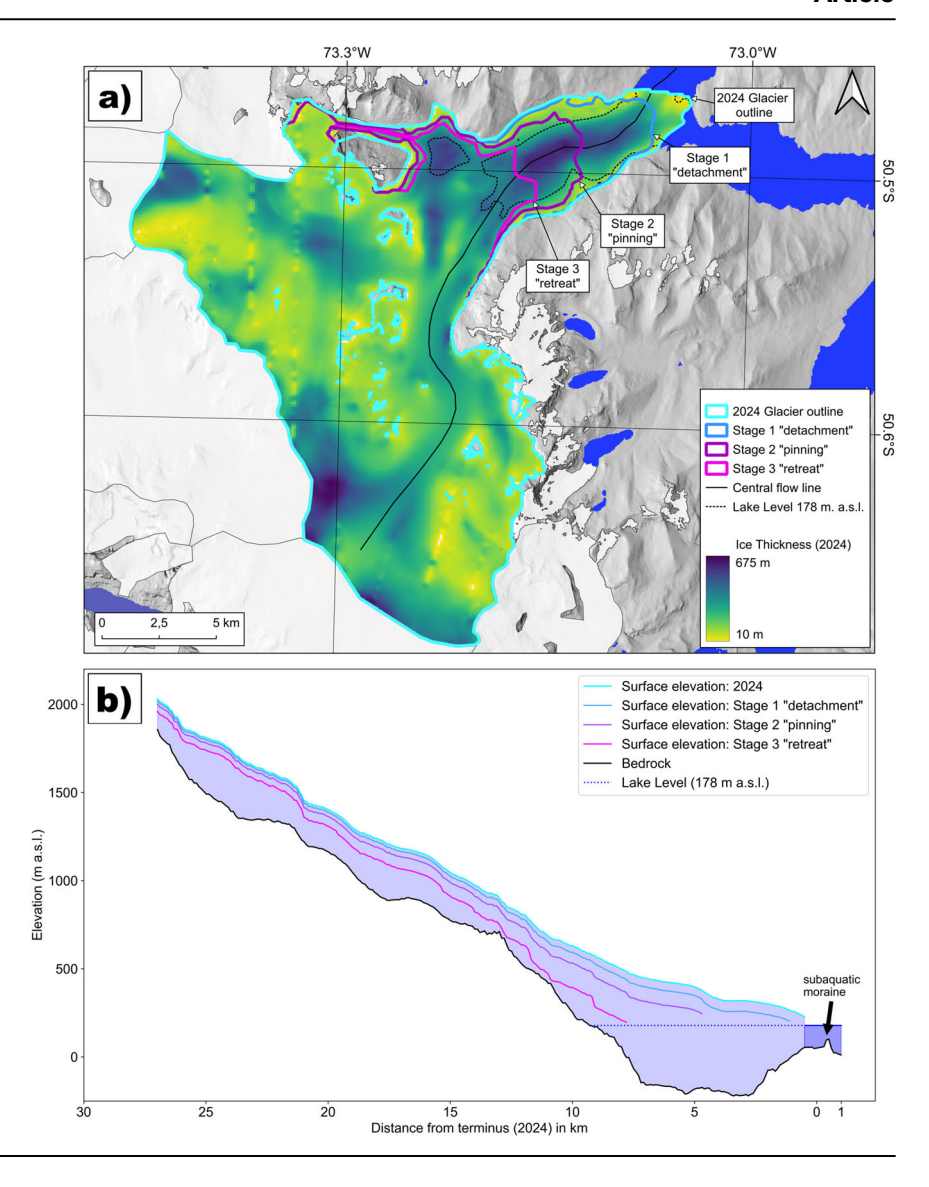
Fig. 2 | Surface elevation change rate, surface lowering since 2000 and surface velocity timeseries. a Ice surface elevation change rate map of the Glaciar Perito Moreno derived from TanDEM-X DEMs for the period 2019 to 2023. Hatched areas indicates data gaps. The solid black line indicates the central flow line as a reference profile. Black crosses represent the surface velocity extraction points V1-V4. Background: SRTM hillshade. b Surface elevation time series along a central flow line of Glaciar Perito Moreno. Date refers to the median acquisition time. The reference year is the SRTM DEM from 2000.02.16 (0-line). The light grey bar plots indicate the surface elevation. We discarded elevation information within the first 1500 metres due the glaciers retreat until 2024. c Surface velocity evolution from 2015 to 2023 at points V1-V4 along the central flow line. Each dot represents an individual measurement, and solid lines are weighted moving



Témpanos. At this location, the bed elevation is approximately 50 m a.s.l., with an ice thickness of \sim 190 m. In the central part of the glacier tongue, where the ice is thinnest, the red line (Fig. 1b) marks a small area to the north that lies above lake level. Despite the glacier's thinness at this location, field observations of calving events indicate that it is grounded below lake level. Toward the Brazo Rico in the south, the bedrock does not exhibit a well-defined glacial trough. Approximately 1.5 km up-glacier, however, a distinct retrograde slope descends into a deep basin. The bed elevation in this central part of the glacial trough is 200 m below sea level. Here, the ice thickness

increases from 200 m to 500 m (see Fig. 3a). This overdeepened segment of the glacial trough extends for an additional 5 km farther upstream. There, a constriction occurs where a ridge extends 1.5 km into the valley from the southern margin, narrowing the flow path. This location also corresponds to the point of maximum ice thickness, measured at approximately 700 m. These observations are in agreement with seismic measurements of 703 ± 35 m in 1996^{20} . Further upstream, 9.5 km from the 2024 terminus, the bed elevation surpasses the current lake level along a prograde slope. Here, the glacier surface broadens due to the convergence of ice flows from higher

Fig. 3 | Reconstructed ice thickness distribution and glacier retreat stages. a The reconstructed ice thickness (2023) of the Glaciar Perito Moreno based on GPR measurements carried out in 2022. Current outline (2024), as well as the outlines throughout stages 1 to 3, are shown. The lake level is indicated by the dotted black line, and the solid black line indicates the cross section shown in (b). Background: SRTM hillshade and SRTM water body mask. b Cross section of the glacier displaying the current surface elevation as well as surface elevations and frontal positions of stages 1 to 3.

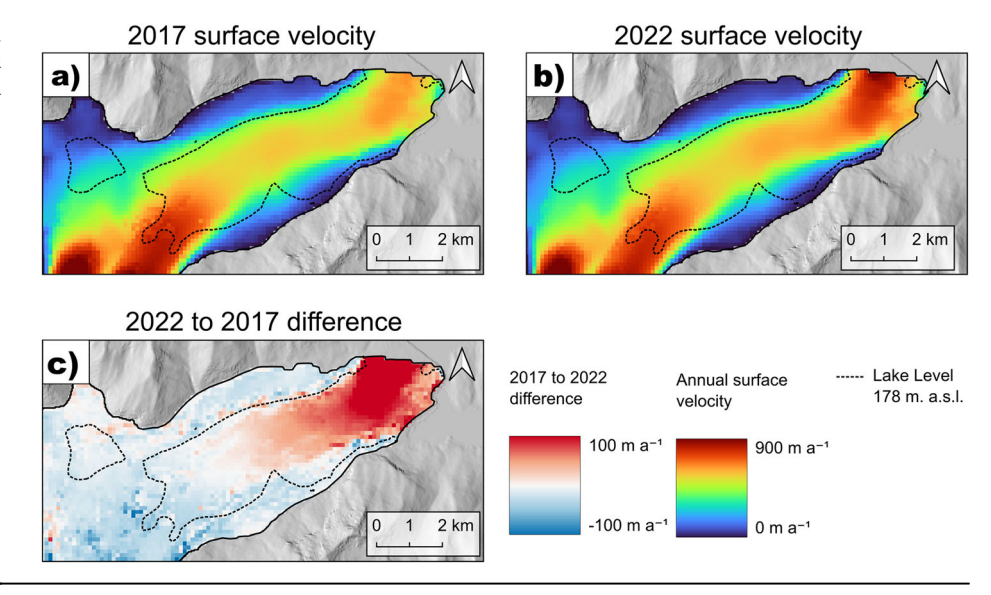


elevations. In the branch extending to the south, our observations indicate that the ice is flowing through two prominent channels. These subglacial channels are separated by a 300-metre-high bedrock ridge. The formation of this ridgeline is attributed to the inflow of extensive ice masses from the accumulation zone from the north-eastern part of the glacier, which subsequently flows into the host valley.

In March 2023, bathymetric measurements were conducted in the vicinity of the northern glacier front in the Canal de los Témpanos, with a particular focus on the recently ice-free area. The observations revealed a terminal moraine coinciding with the last maximum positions of the glacier ice front in the Canal de los Témpanos in 2003/2004 and 2011/2012. During these particularly strong advances the glacier tongue also dammed the Brazo Rico elevating its lake level by more than 9 m²⁰. The terminus retreated only ~50 to 100 m from this position until 2019 (Fig. 1b, c). The subaqueous moraine reaches heights of 100 to 120 m above the general lake floor elevation. It forms a sill that determines the temperature stratification of the water in proximity of the glacier³⁶. This phenomenon controls to the circulation and stratification of water in the vicinity of freshwater calving glaciers. The processes are governed by density disparities between colder glacial meltwater and warmer lake water, which are themselves contingent upon temperature, pressure, and sediment concentration^{22,36}. The cold and turbid water in front of Glaciar Perito Moreno is confined to the depth of the bathymetric sill, while only the upper water layers are subjected to heating by solar radiation and wind-induced mixing. As a result, subaqueous melt is diminished at depth³⁷. After 2020, however, a pronounced recession was observed at the north-western lake shore of the Canal de los Témpanos. There, the terminus retreated 800 metres within a period of only four years. The fastest retreat occurred along the deepest part of the trough. Retreat at the eastern terminus towards Brazo Rico is less pronounced. However, since 2019, the terminus has also retreated between 200 and 400 m. For this segment, this is the most pronounced retreat observed in recent decades.

To observe changes in the surface elevation of Glaciar Perito Moreno, we analyze time series of synthetic aperture radar (SAR) DEM acquisitions between 2000 and 2024. The cloud and illumination independence of radar imagery is of particular advantage in a notoriously cloudy region like Patagonia. For the year 2000, the Shuttle Radar Topography Mission (SRTM) Digital Elevalation Model (DEM) was used. For each year 2011 to 2024, we used TanDEM-X elevation models (Fig. 2a, b)³³. The date in Fig. 2b refers to the median date of all stacked DEM scenes used for that year. We selected only scenes at the end of austral summer, which is also close to the acquisition time of SRTM. The mean DEM-differencing error for the SRTM to TanDEM-X elevation models is ±0.09 m a⁻¹ on stable terrain, averaged over the entire observation period. In the case of the change between 2019 and 2023 using TanDEM-X DEMs, the uncertainty was ± 0.35 m a⁻¹ (detailed information can be found in the supplementary material in Supplementary Tables S1, S2 and S3). Figure 2a shows the 2019 to 2023 elevation change rate. The results show an overall negative ice elevation change rate over almost the entire glacier domain. Throughout the accumulation

Fig. 4 | Surface velocity maps and 5-year evolution. a, b Annual surface velocity mosaics from 2017 and 2022. c Change in surface velocity between 2022 and 2017 in m. Data source: ITS_Live. Background: SRTM.



zone, one can observe negative elevation change rates of $-0.7 \,\mathrm{m~a^{-1}}$ to $-1.2 \,\mathrm{m~a^{-1}}$. Towards the terminus, the glacier surface lowers at an average rate of up to $5.5 \,\mathrm{m~a^{-1}}$. However, this surface lowering is not uniform. The highest rates, exceeding $6.5 \,\mathrm{m~a^{-1}}$, occur along the deepest glacial troughs near the terminus. In contrast, areas where the ice rests on shallower promontories show lower rates of about 3 m a⁻¹.

To assess the temporal evolution of the elevation change, we extract the elevation of the SRTM DEM from 2000 and the TanDEM-X elevation data from 2011 to 2024 along the flowline (Fig. 2b). It shows small changes in surface elevation along the centerline between 2000 and 2011. However, it should be recognized that SRTM data are susceptible to bias in high mountain regions due to signal penetration in dry snow, which was likely present at the time of acquisition³⁸. The ablation zone of the glacier is likely not affected by the penetration bias due to the acquisition taking place during February, when the ablation zone of the glacier is snow free. In the subsequent eight-year period leading up to 2019, a gradual reduction in ice surface elevation was observed. However, no discernible acceleration in the rate of surface lowering occurred. In the lower ablation zone, surface lowering was limited to approximately 5 m, implying rates of less than 1 m yr⁻¹. From 2019 to 2022, thinning rates increased by a factor of 5 to 7 (see Supplementary Tables 2 and 3 and Supplementary Figs. S1, S2, S3, S4 and S5 for a detailed uncertainty analysis). This trend intensified through 2024. In addition to the considerable surface lowering observed in the glacier's ablation zone, elevation decreases are also evident in the accumulation zone $(\sim 4-5.5 \text{ m yr}^{-1} \text{ below and } 0.9-1.2 \text{ m yr}^{-1} \text{ above the equilibrium line altitude}$ [ELA] at 1200 m a.s.l.). By 2024, substantial lowering was confined to lower elevations (below ~1500 m a.s.l.), while surface lowering at higher elevations was barely detectable. This pattern may be explained by increased accumulation during autumn and winter 2023-2024, likely caused by the strong El Niño event³⁹.

As shown in Fig. 2c, the evolution of surface velocity reveals corresponding speed increases near the glacier terminus. Surface velocities were extracted at four points (V1 to V4) along the flow line, as depicted in Fig. 2a. V1 (purple) is closest to the terminus (see Fig. 1a), while V4 (red) is located approximately 16 km upstream. The highest velocities of ~1250 m a⁻¹ were recorded at V4, where most of the ice mass flows through a narrow, 2 km wide passage. As the glacier geometry widens, surface velocities at V3 (blue) decrease to an average of around 800 m a⁻¹. Seasonal flow acceleration patterns from 2018 onwards peak during the summer months. The two points closest to the terminus, V2 and V1, show similar ice flow rates from 2015 until the winter of 2018/2019. Thereafter, a gradual increase of the surface velocity near the terminus can be observed. From 2021 to 2023 surface velocities at V1 reach almost 900 m a⁻¹. A less pronounced but also

visible acceleration can be observed further upstream at V2. Notably, these accelerations are not observed at V3 and V4. The observed increase in frontal surface velocity indicates a dynamic adjustment towards the glacier tongue gradually propagating up glacier. The enhanced glacier flow may result from a reduction in effective pressure at the bed due to thinning; however, other factors, such as decreased buttressing from separation from the subaqueous frontal moraine or the advance into deeper water, could play an equal or even more important role. While reduced effective pressure would act immediately across the thinning area, changes in buttressing are likely to trigger a dynamic response that propagates upstream from the terminus, consistent with observed flow acceleration patterns.

The Fate of Glaciar Perito Moreno

To project potential stages of the future retreat of the glacier, we set up a simple, conceptual numerical model that is forced by the 2019–2023 elevation change rate and calving due to the buoyant force distribution exerted by the water (see Methods). Rather than making explicit predictions on a timescale, the aim is to identify glacier retreat stages based on our observations. This scenario implicitly assumes that current thinning rates will prevail throughout all iterations of the model run (Fig. 3a, b). Whilst the model does not incorporate a physically based calving solution, it does capture buoyancy-driven calving by comparing the buoyant condition of each ice column after each iteration of surface lowering 40, since it is widely acknowledged that buoyant forces at lake-terminating glaciers play a pivotal role in glacier retreat in the region 12,25. The results presented herein demonstrate the potential for future glacier retreat, as based on our obtained bedrock information.

Potential stages of future frontal retreat of Perito Moreno are shown Fig. 3. As previously mentioned, the stages are the result of continuous elevation-dependent ice surface lowering and subsequent calving after the ice surface has surpassed its buoyant threshold. The initial state is the current 2024 glacier outline. Stage 1 in this sequence is defined by the detachment from the subglacial bedrock ridge at the glacier front. The model demonstrates an increase in retreat rates from both Brazo Rico and, more pronounced, the northern Canal de los Témpanos as the glacier continues to thin. Once the central part of the glacier front retreats into lake depths similar to those of the Canal de los Témpanos, the bedrock ridge will no longer act as a pinning point. At this stage, the resistive stresses from this basal pinning point are no longer stabilising the glacier front. The ice masses will be in close proximity to or at flotation, thereby reducing the effective pressure at the glacier bed. This results in an increase in basal sliding, leading to higher ice velocity (not captured in our conceptual approach), which in turn increases the thinning rate in proximity to the terminus. Similar

processes have been reported for other large outlet glaciers in the region, such as Glacier Upsala, O'Higgins, Viedma or Jorge Montt 12,13,41,42. This process ultimately leads to enhanced buoyancy-driven calving. The selfsustaining nature of this positive feedback loop, when considered in combination with the steep retrograde aspect of the slope, strongly suggests the potential for rapid glacier retreat. The ongoing retreat phase is projected to continue until Stage 2, owing to the widening of the glacier geometry and the persistence of a deep glacial trough. In this area, the ice is found to be at its thickest (~700 m), and a constriction measuring 1 km in length is present at the southern margin. The latter could function as a new pinning point, thereby exerting stability on the glacier front and reducing the ice surface area in contact with water. This will, in turn, also reduce subsurface melting. The presence of greater amounts of ice above the lake level serves to reduce the likelihood of the glacier attaining a buoyant state. The duration of the glacier front's presence at this stage is contingent upon the surface mass balance of the glacier, a factor which has not been incorporated into the model. While the model demonstrates that in the long term the glacier would retreat beyond this point as a consequence of continuous surface lowering, the impact of the surface mass balance remains to be taken into consideration. In the event of the glacier undergoing continuous surface lowering at this stage, a second retreat Stage 3 is to be anticipated. This subsequent retreat is hypothesised to decelerate as the glacier bed becomes prograde, thereby gradually reducing the buoyant force of the water and the melt rates below lake level.

Discussion

The glacier surface elevation datasets - presented here - reveal that the glacier is losing mass at an accelerated rate across its entire ablation zone. Should glacier thinning continue at this rate, a substantial portion of the glacier terminus will become buoyant, particularly within the first 5 km upstream from its current-day front. Here, we can observe a fragile balance between the local elevation of the glacier surface above lake level and the local lake depth. In the lower ablation zone in proximity to the glaciers terminus, a 16fold increase in surface lowering rates were observed between 2019 and 2024 in comparison to the 2000 to 2019 period. In good correspondence with that, we have identified patterns of surface velocity increases during that period. As shown in Fig. 4a and 4b, these fast-flowing areas coincide well with areas grounded below or at lake level. It is hypothesised that the increase in velocity is attributable to a decrease in effective basal pressure and reduced lateral stresses. Similar periods of fast retreat have been reported to be associated with increased calving activity and speed-up near the terminus of other Patagonian outlet glaciers 10,12,24,43. For example, the glaciers Viedma, Upsala and O'Higgins have also undergone stages of enhanced retreat after detaching from previous pinning points^{12,41,44}. At Glaciar Perito Moreno, the observed pattern of surface velocity increases since 2022 is particularly pronounced in areas where the glacier is grounded below lake level. In these regions, the reduction in effective pressure resulting from a decrease in glacier thickness leads to an acceleration of ice flow. The areas with the strongest increases in ice speed clearly coincide with those located below lake level, while the regions above lake level experience comparatively slower ice flow. The observation of an increase in annual velocities of more than 100 m a^{-1} at the glacier's terminus, while a reduction of ~50–70 m a^{-1} is visible at the inflow to the lower ablation zone and above lake level, indicates that the glacier is not only losing mass at its terminus but also that less mass is being transported from the accumulation zone. This supports the hypothesis that the glacier will continue to thin. If current calving rates persist, the glacier is likely to retreat toward the retrograde bed slope, where a large-scale retreat is anticipated once the stabilizing influence of the subglacial bedrock ridge is lost. Furthermore, as the glacier retreats further into deeper bathymetry, a greater portion of its ice will come into direct contact with lake water. This retreat will, in turn, enhance subaqueous melting at the glacier front and to enhanced calving. To quantify this effect, we calculated the change in the area below lake level from the current (2024) glacier front to four downstream cross sections (see Supplementary Fig. S8b-e and Supplementary Table S4). Near the initial retreat stage (cross-section 1, see Supplementary

Fig. S8b), the submerged area has already increased by approximately onethird compared to its extent in 2024. Cross Section 2 is roughly halfway between stage 1 "retreat" and 2 "pinning", where the glacier trough has reached its maximum depth. The subaqueous frontal area at this stage is increased by 90.76%. At cross Section 3, located at the valley constriction, where we expect a phase of stability, the area decreases by approximately 35% compared to cross Section 2. Water temperature measurements in austral summer 2013 in both lakes revealed near surface temperatures of 7 to 6 °C and 5.9 to 5.4 °C at depth in Canal de los Témpanos and Brazo Rico, respectively³⁶. Since the glacier front is no longer directly at a subaqueous moraine, also deeper lake layers will experience warming due to winddriven mixing^{36,37}. Unlike to marine terminating glaciers, the cold and turbid water discharged by lake-terminating glaciers stays at the lake bottom³⁶. Warmer surface layers increase melt rates at the glacier front, which will likely destabilize the glacier front further and subsequently triggers buoyancy-driven calving⁴⁵.

In regard to the past stability of Glaciar Perito Moreno, our observations show that the glacier rests on a pronounced ridge that stabilizes the tongue both towards Brazo Rico and Canal de los Témpanos. In addition, the subaqueous moraine - present in the Canal de los Témpanos - acts as a sill and limits exchange of water masses and heat with the lake, thus reduced subaqueous melt rates at the glacier front. In the past, the moraine prevented cold and turbid water from flowing further into the proglacial lakes (Lago Argentino and Brazo Sur), and consequently reduced melt rates at depth. We suspect that a similar moraine may exist in Brazo Rico, but glacier advance was less pronounced than in Canal de los Témpanos. The presence of a moraine in contact with the glacier front also exerts buttressing stresses on the glacier front, thereby enhancing its stability. Consequently, this phenomenon leads to a reduction in both the frequency of calving events and the typical amount of the mass discharged during each event. Apart from the protective bathymetric setting and the promontory plug, Glaciar Perito Moreno is stabilized by lateral topography that converges towards the glacier front. A final argument for the past glacier stability is the vast and high accumulation area above the ELA at 1200 m a.s.l.⁴⁶.

Uncertainties of the DEM-derived elevation changes can result from time-varying depths of X-band penetration⁴⁷. Therefore, we exclusively select SAR DEMs of the southern hemisphere ablation period when penetration depths are small due to widespread surface melt across the glacier domain⁴⁸. We then stack these DEMs and calculate the median elevation of each raster stack, which serves to mitigate the effects of residual interferometry, co-registration, and penetration artefacts that may be present in individual scenes. Furthermore, GPR data is subject to inherent uncertainties. It is important to acknowledge that certain errors are challenging to resolve during the processing stage. These include multiple reflectors in proximity to the glacier margin and the ambiguity of reflectors in conjunction with increasing ice thickness⁴⁹. Since the campaign was conducted at the end of the austral summer, the presence of a snow layer above the solid ice of the glacier, which could have influenced the speed of wave propagation, is not expected to introduce many disturbances. The air layer between the antenna and the glacier surface was taken into consideration. A velocity model was created for each subset of the flight, incorporating the air and ice layers for the diffraction analysis. Positioning errors due to GPS uncertainty were also addressed (see Methods). We find three major sources of uncertainty in our profiles (see Supplementary Fig. S6), which contribute to errors in the range of ~10% in thickness values. They are likely associated with steep slopes near the glacier margin, water content in temperate ice, thick ice cover, and surface roughness (e.g., deep crevasses). The reconstructed thickness map inherits further errors from the mass conservation approach stemming from uncertainties in the input fields. We therefore expect larger errors with increasing distance from the point thickness measurements. Yet, these errors remain well constrained by the dense survey grid. Moreover, we consider the pattern of the thickness distribution to be robust and have high confidence in the presence of the over-deepened bed section — albeit with less certainty regarding the absolute values of local ice thickness. Nonetheless, our observations align well with previous borehole and seismic measurements^{20,25}. The bedrock elevation determined at a borehole ~4 km from today's terminus in 2011 was 380 m below lake level²⁵. Our nearest measurements indicate elevations of approximately 350 to 360 m below lake level, providing additional confidence in the overall accuracy of our results. Finally, we would like to address the potential limitations of the buoyancydriven model results presented here. The model itself only compares ice overburden pressure to buoyancy forces exerted by the adjacent water column. Although buoyant forces are known to trigger full-depth calving⁵⁰, we do not account for ice-dynamic adjustments. In particular, we neglect the effects of changes in longitudinal and transverse horizontal shear stresses. While we currently observe retreat rates of several hundred metres per year at the northern margin of Glaciar Perito Moreno, we did not impose a retreat rate in our results. Additionally, we presume a constant surface lowering rate based on the elevation change rates measured between 2019 and 2023. The time series analysis has shown that the increase in surface lowering is not linear and therefore, an increase in thinning due to the dynamical adjustment close to the glacier front is a reasonable assumption. Since our model is forced with the 2021-2023 surface lowering rates, it captures the primarily dynamically driven thinning during this period, but does not impose any further acceleration resulting from positive feedback mechanisms. This assumption could be an overestimation, given that 2022/ 2023 was an extremely hot summer in Argentina⁵¹. The assumption of linear surface lowering rates does not allow direct quantitative statements and should therefore only be understood as a first approximation of possible retreat phases that the glacier could go through. A limitation of this approach is that it does not account for mass movements or changes in surface mass balance beyond elevation-dependent surface lowering. Consequently, the ability to determine if the glacier is in equilibrium at any given point, such as at the aforementioned valley constriction, is precluded. It is acknowledged that more sophisticated modelling approaches exist, which account for mass movement, temporal changes in surface mass balance, elevation feedbacks, and incorporate updated glacier geometries and thickness fields. These approaches allow for the correction of the elevationdependent surface lowering field to be incorporated^{28,52-54}. The efficacy of such approaches has been demonstrated for lake-terminating glaciers in Alaska, as they facilitate the modelling of ice dynamical feedbacks under future scenarios⁵⁴. However, such models rely on climate variables, particularly temperature and precipitation, as inputs to calculate the surface mass balance of the glacier⁵⁵. In Patagonia, precipitation estimates vary considerably and no direct measurements on the plateau are available. The precipitation at higher elevations therefore remain a largely unknown component for one of the wettest regions on Earth⁵⁶. The effect of the general overestimation of accumulation rates has been thoroughly discussed⁵⁷. A noteworthy discrepancy exists between modelled surface mass balances using climate data^{7,58-60} compared to mass balances from geodetic approaches, which tend to be more negative 1,4,9,11,48,61. It has been hypothesised that this discrepancy can be attributed to an overestimation of precipitation in Patagonia^{56,62}, a phenomenon that persists even in regional climate models⁵⁷. A study modelling the SMB of the Southern Patagonian Icefield until 2050 corrected their modelling results with frontal ablation estimates and still found a marginally positive projection under the Representative Concentration Pathway (RCP)2.6 pathway and only a slightly negative one under RCP8.5⁵⁷. Based on current projections for the region, temperatures and surface melt are expected to continue to increase⁵⁷. That being said, for the ice thickness reconstruction from which we derived the bedrock topography, we also use an existing SMB product as input⁷. While uncertainties in the SMB field do affect the accuracy of the ice thickness reconstruction, sensitivity studies conducted in prior work have shown that even poorly constrained SMB products do not significantly reduce the accuracy of the reconstruction method, provided the area is well constrained by observational (ice thickness) data⁶³. In our study, the dense survey grids offer strong constraints, enabling a reliable reconstruction of the ice thickness field. Nonetheless, in the central part of the glacier front toward the north, our reconstruction yields comparatively thin ice values. When deriving the bedrock topography, these areas then appear to lie above lake level (see Fig. 1b). However, field observations show that this is not the case. We believe this discrepancy is largely due to the relatively low ice velocities in this area, which result in thinner ice values during the second step of the ice thickness reconstruction. Additionally, the measured ice thickness of 50-60 m here likely leads to an underestimation. The latter can be attributed to the presence of extremely large and deep crevasses in this specific part of the glacier. These features introduce complex scattering, attenuation, and signal delay effects that reduce the accuracy and reliability of the data. Such effects can lead to an underestimation of ice thickness, which subsequently propagates into the ice thickness reconstruction. With regard to the oscillating ENSO phases, Glaciar Perito Moreno will continue to experience substantially more winter accumulation every few years. However, it has been observed that the positive effect of higher snowfall in winter is rapidly diminished by extreme surface melt rates in the subsequent summer season. Additional factors like strengthening of foehn-type events^{64,65} and hence a better understanding of surface mass balance and its temporal changes and variability need to be addressed in order to accurately forecast future behaviour of Glaciar Perito Moreno. Nonetheless, our findings highlight the fragile balance of one of the most well-known glaciers worldwide.

This study presents a unique dataset compiled for one of the most visited glaciers worldwide that may well be on the verge of collapse. For the first time, we present a dataset that unveils the bedrock topography of Glaciar Perito Moreno, a valuable data source for modelling approaches and future glacier projections. Our bathymetric study shows maximum advances of the glacier in the Canal de los Témpanos, which coincide with a subaqueous moraine. The presence of such has added stability to the glacier front in the past. However, recent observations have revealed a retreat of more than 800 m in this area. This retreat coincides with surface lowering rates of up to 5.5 m a⁻¹ visible in the last four years of a 24-year elevation record. Furthermore, we extrapolate present lowering rates to the end of this century and allow for glacier retreat due to buoyant calving, a process that has been well studied on glaciers with similar bed topographies of the study gains in prominence because the glacier is undergoing its most substantial retreat in the past century as of the writing of this paper (2025)⁶⁷.

Methods

Ice thickness measurements and processing

Ground penetrating radar (GPR) data for this study were acquired in March 2022. During three survey flights, 120 km of bedrock topography was surveyed using a 25 MHz centre frequency broadband bistatic radar suspended below a helicopter ⁶⁸. The system was operated at ~60 km/h true air speed, approximately 15–20 m above ground. GPR data was collected at a sampling interval of 10 Hz, corresponding to ~2 m horizontal increment per trace. Georeferencing was done using two Leica GS16 multifrequency Global Navigation Satellite System (GNSS) receivers. The GNSS antenna (rover) was centrally mounted on the radar antenna, while the GNSS base station was mounted in proximity of the Helicopter take-off and landing area (see Supplementary Fig. S7). The differentially processed GNSS data were later on matched to the GPS and clock of the GPR system and combined with the GPR data sets. The GPR data were processed with the REFLEXW v8.5 software by Sandmeier Geophysical Research, applying the process detailed below:

First, the data was repositioned into equidistant traces, since subsequent filters calculating migration require equidistant traces. We then subset the data strips with partial overlap to reduce the processing time. The strips were later joined into a single vector containing all data points. A time shift to the traces was applied for zero time of the radar. To remove coherent noise in the data, a spatial average (of 201 traces) is calculated and subtracted from each trace. This step aims to remove "background noise" present in the data. We removed high-frequency radio noise and spikes by filtering with a bandpass filter of 10 MHz for the low and 40 MHz for the high end cutoff. We applied a gain function to compensate for geometric and absorption losses along the ray path and a further enhancement of small amplitudes using an average energy decay function. The amplitude is based on a mean amplitude decay curve automatically determined from all traces of the

section. In order to account for the phenomenon of diffraction, it is necessary to determine the air and ice layers. This is achieved by manually delineating the surface reflections and subsequently creating a two-dimensional model consisting of an air and ice layer for each subset. For the air layer, the wave propagates at the 0.3 m/ns. For the ice layer, we assumed a constant velocity of 0.168 m/ns. With the created 2D-velocity model, we applied a 2D-migration of the previously processed data by diffraction stacking, thus focusing scattered amplitudes for better interpretation. Subsequently, given the air distances from the air layer, each trace was statistically corrected, i.e., each trace was shifted up to negative times in the y-direction. Finally, we interpreted the profiles and picked the two-way-travel times in ice, converting them into thickness along the profiles. We finally merged the results of all data blocks into a single vector.

Ice thickness reconstruction

To map glacier ice thickness between the actual survey lines, we applied an established state-of-the-art ice thickness reconstruction method 32,63,69. It is primarily based on mass conservation and has successfully been applied to several regions^{31,32,69}. As the observations serve as a constraint for the model, they increase the accuracy of the ice thickness distribution in the lower areas of the glacier. Besides our observations, which cover the majority of the ablation zone, thickness values along airborne gravity survey flightpaths in the accumulation zone were extracted and used as input⁷⁰. Reference outlines were taken from the Rudolph Glacier Inventory version 6 (RGI6.0)⁷¹. Surface elevation and elevation change maps were based on the 30-m product of the Shuttle Radar Topography Mission (SRTM, v2.1)³⁴. Elevation change rates are based on subsequent TerraSAR-X-Add-on for DigitalElevation Measurements (TDX)³³ for the timestamps 2011, 2016, and 2019. The surface mass balance data is statistically and dynamically downscaled NCEP-NCAR atmospheric reanalysis data (1965-2011)^{7,72}. Based on that data, the glacier SMB was derived using an enhanced temperature index model for cloud-cover corrected potential incoming radiation³¹. Velocity fields for the second step of the reconstruction and to estimate the frontal ablation and frontal ice discharge, existing region-wide mosaics were used⁷³. Fluxgates were placed close to the present-day terminus position. The ice flux is computed as a product of the ice thickness and the surface velocity component perpendicular to these gates. The ice thickness is initially reconstructed based on the year 2000 SRTM DEM. We then update the outline and surface elevation to derive the ice thickness distribution of the year 2023 based on Sentinel-2 and TanDEM-X data.

In the first step, we utilize two different strategies to infer the glacierwide ice thickness fields (without surface velocities)^{32,63}. First, we apply an iterative flux-based method. This method formulates the problem in terms of ice flux, which is then converted using the Shallow Ice Approximation (SIA). This conversion is dependent on a spatially variable viscosity parameter, which is estimated in areas with existing thickness data. This classical method was updated with a viscosity re-scaling, which improves the thickness distributions further away from observations⁶⁹. The second approach is based on the perfect plasticity assumption (PPA)⁷⁴. This method assumes that the driving stress (τd) equals a material-dependent yield stress (τ_0) . τ_0 is determined at points with observations and interpolated across the glacier domain. To include effects of non-local stress transmission⁷⁵, the driving stress field is smoothed spatially, first with a constant-radius kernel and then updated once⁶³. The thickness field from these methods then acts as boundary conditions for the second step. Here, the thickness field is directly refined with regions where surface velocities exceed 100 yr⁻¹. The two thickness maps are then averaged to infer a multi-model estimate³¹. The triangular model mesh has a 400 m resolution, which is refined to 200 m near measurements. For the final thickness map, results are then interpolated to a 200 m rectangular grid.

Bathymetry survey

In order to retrieve the bathymetric data of the pro-glacial lake, we used a Lawrence Elite 7 FS sonar operated with an 80 kHz frequency-modulated Airmar B75M transducer. Several depth profiles were gathered during a

field campaign on March 30, 2023. These were subsequently processed in the software Reefmaster 2.0. We manually delineated the sonar signal to derive the lake bed as vector points.

Glacier outlines

The position of the terminus for each year from 2000 to 2024 was manually derived from Landsat 7 and Sentinel-2 optical imagery. The frontal position of each year was manually delineated from cloud-free acquisitions in April of each corresponding year. For the years 2003 and 2011, we used November scenes, since we wanted to capture the maximum extent of the glacier front at the end of the austral winter. The glaciers advanced during those two years likely formed the subaqueous moraine in the Canal de los Témpanos. The timing of the maximum extents was described prior 18.

Glacier surface elevation change

For the observation of time-varying glacier surface elevations, we use coregistered Single look Slant range Complex (CoSSC) data of the TerraSAR-X add-on for Digital Elevation Measurement satellite (TanDEM-X) of the German Aerospace Centre (DLR). The bistatic TanDEM-X mission provides high-resolution Synthetic Aperture Radar (SAR) X-band data products⁷⁶, which are acquired independently from pervasive cloud coverage in Patagonia. In 2011 and 2024 several scenes were available covering the entire glacier basin. Whenever possible, we selected SAR acquisitions of the southern hemisphere ablation period to minimize elevation offsets due to time-varying depths of signal penetration into the glacier volume and differences in snow and ice accumulation.

Digital Elevation Models (DEMs) were created from each TanDEM-X acquisition using SAR interferometry following an established workflow⁴. Initially, acquisitions in the along-track direction were concatenated and differential interferograms were calculated, unwrapped using a minimum cost flow algorithm, and converted to elevation values on a reference surface DEM. As a reference surface, we used the void-filled Shuttle Radar Topography Mission (SRTM) DEM at 1 arcsec spatial resolution, which was acquired during February 2000³⁴. Thereafter, the "raw" TanDEM-X DEMs are 3-dimensionally co-registered to the SRTM DEM on all stable terrain with less than 25° surface slope, excluding glacier and water areas. We applied an iterative process using the terrain slope and aspect-based universal co-registration approach⁷⁷ and a bilinear least squares correction¹¹ to minimize horizontal and vertical shifts, respectively. To further increase the quality of our DEMs we have removed erroneous processing artefacts. These include outlier cells from layover/shadow estimation, which is an effect common before and behind steep terrain (in azimuth), the unwrapping of the interferometric phase, which describes the process of restoring the correct multiple of 2π to each point of the interferometric phase. Finally, we masked out the land area, with unrealistically high vertical deviations (+ −100 m) from the SRTM reference surface. The acquisition date of each TanDEM-X scene was stored alongside the respective DEM to estimate the cell-specific observation period. To improve the spatial coverage of the glacier surface and further reduce uncertainties due to vertical biases caused by remaining processing artefacts or variations in signal penetration between DEM acquisitions, we have aggregated DEMs of the southern hemisphere ablation period, which have been acquired -whenever possiblewithin time intervals of less than 60 days prior or after the SRTM mean acquisition date (February 16th). Thereby, the surface elevation of Glaciar Perito Moreno during the ablation period was estimated from repeated SAR acquisitions between December 18th and April 16th for the years 2012-2014, 2019, 2023 and 2024. For the remaining observation years (2011, 2017, 2018, 2022), we used all available DEM data due to the lower temporal coverage. The selected, contemporaneous DEMs were stacked and the median elevation and acquisition date was calculated for each cell. The following section provides a comprehensive overview of the available digital elevation model (DEM) products. In addition, it details the creation of multi-temporal elevation mosaics, as well as the derivation of median acquisition dates. This information can be found in Supplementary Table S1. The mean vertical elevation deviation of all aggregated SAR

acquisitions, i.e., the average difference between the highest and lowest elevation value of each raster cell and each group of stacked DEMs (Supplementary Table S2), respectively, range from 0.2 m (2013 DEM stack) to 11.4 m (2024 DEM stack). Eventually, vertical changes of the glacier surface are estimated by differencing the co-registered SRTM and TanDEM-X DEMs and are converted to maps of elevation change rates $(\Delta h/\Delta t)$ based on the cell-specific observation period. In addition, we calculated the total vertical change relative to the SRTM DEM by extracting mean elevation changes along the buffered (150 m) main flowline of GPM within segments of 500 m distance each.

Our error budget (Eq. 1) of the interferometric elevation change calculation ($\delta_{\Delta h/\Delta t}$) considers uncertainties from the relative vertical precision of the DEM-differencing on stable terrain ($\sigma_{\Delta h/\Delta t\,AW}$), spatial autocorrelation (S_{cor}) and variations in SAR penetration depth (S_{pen}).

$$\delta_{\Delta h/\Delta t} = \sigma_{\Delta h/\Delta t AW} \times \sqrt{\frac{S_{cor}}{5 \times S_G}} + S_{pen} \tag{1}$$

To estimate remaining deviations on stable terrain, we select all elevation change values, excluding glacier and water areas, within a 10 km buffer radius based on the outline of GPM provided by the Randolph Glacier Inventory 7.0⁷⁸. Elevation change values of the selected cells are then aggregated within 5°-slope bins and filtered by the 1-99% quantile. Thereafter, the vertical accuracy is calculated as the standard deviation of each slope bin and weighted by the respective slope bin distribution on glacierized areas ($\sigma_{\Delta h/\Delta t~AW}$). The slope-based mean vertical offsets on stable terrain are shown in Supplementary Fig. S1. To account for spatial autocorrelation, we derive an average lag distance (d_1) of ~700 m from semivariograms of 100,000 random stable terrain $\Delta h/\Delta t$ samples to derive the correlation area (S_{cor}) and glacier area (S_G) multiplied by an empirical weighting factor of 5 as proposed by a previous study⁷⁹. The depth of the SAR signal penetration into the glacier volume is related to the prevailing surface conditions at the acquisition time. Penetration depths are small during melt conditions but can increase up to ~10 m at high elevations when the glacier surface is dry and frozen⁴⁷. While the majority of the SAR DEMs have been acquired during the southern hemisphere ablation season with widespread surface melt across the glacier and therefore likely small penetration depths, the derived elevation change rates $(\Delta h/\Delta t)$ might be biased by time-varying penetration differences. However, our analysis of the interferometric coherence of the TanDEM-X bistatic SAR (Supplementary Fig. S2) shows little change in the distribution of coherence across GPM, with relatively high coherence values for the majority of DEMs. A relative loss of coherence is only observed for a limited number of DEMs (e.g., DEM acquisition 2013-03-02), indicating the presence of multiple scatterers within a resolution cell ("volume decorrelation") and therefore potentially higher penetration depths^{80,81}. It is also worth noting that the magnitude of coherence loss due to volume scattering is related to the height of ambiguity (HoA)⁸¹, which is controlled by the SAR acquisition geometry. At Glaciar Perito Moreno, a number of DEMs have been acquired with relatively large HoA (>200 m), which can result in less decorrelation of the total interferometric coherence but not necessarily smaller depths of penetration by volume scattering (Supplementary Fig. S3). Furthermore, changes in penetration depth may result from the wavelength difference between the SRTM C- and TanDEM-X X-band SAR. However, small penetration depths during the SRTM acquisition were reported previously⁴⁸ for the nearby Northern Patagonian Icefield. Since we cannot estimate the absolute penetration depths of each TanDEM-X acquisition nor the potential differences in C- vs. X-band penetration, we include an assumed linear increase in penetration depth difference (S_{pen}) from 0 m at the glacier equilibrium line elevation of ~1200 m a.s.l.46 to 5 m at the maximum glacier elevation of the study region. The respective stable terrain deviations $(\sigma_{\Delta h/\Delta t\;AW})$ as well as estimated $\Delta h/\Delta t$ uncertainties $(\delta_{\Delta h/\Delta t})$ are summarized in Supplementary Table S3.

Buoyancy-driven retreat model

In order to assess the potential future evolution of glacier retreat, a conceptual tool has been built, focusing on the balance between ice overburden pressure and the buoyancy force exerted by the adjacent water body. For each iteration, we apply average 2019-2023 surface lowering rates $(\Delta h/\Delta t)$ and calculate the ice height above buoyancy. To remove noise, we average our $\Delta h/\Delta t$ -field (Fig. 2a) in 100 m elevation bins. In order to avoid biases, some artefacts were removed prior to averaging. These artefacts mostly comprised areas in the accumulation zone around steep mountain peaks, where geometric effects such as radar shadowing and foreshortening biased our measurements and are indicated as black hatching in Fig. 2a. In this way, we construct an elevation-dependent $\Delta h/\Delta t$ function, which is applied to the evolving surface topography. It inherently accounts for the elevation feedback. We then calculate the relationship of overburdened ice pressure and buoyant forces of water at each point where water is present. As the mass of the glacier is reduced, the mass of the overlying ice is reduced. The flotation elevation h_f is calculated for each glacierised grid point as:

$$h_f = h_b + \left(\frac{rho_w}{rho_i}\right) * (h_w - h_b)$$
 (2)

where h_b is the bed elevation, rho_w the density of water, rho_i the density of ice and h_w is the lake surface elevation. We assumed a density of 1000 kg m^{-3} and 913 kg m^{-3} of water and ice, respectively, and $h_w = 178$ m a.s.l. The height above buoyancy h_{ab} is then calculated as:

$$h_{ab} = h_{DEM} - h_f \tag{3}$$

where h_{DEM} is the surface elevation of each iteration. h_{ab} is calculated for each pixel for every year until 2100, where water is present. We assume a constant lake level of 178 m a.s.l. in that regard. If h_{ab} becomes negative or h_{DEM} is smaller than either h_w or h_b , ice cover is removed from the corresponding areas – thereby simulating calving.

Surface velocities

To assess the evolution of glacier velocities, we retrieved surface velocity data from NASA's Inter-Mission Time Series of Land Ice Velocity and Elevation project³⁵. The data comprises imagery from the Landsat 5–8 satellites missions from 2014 to 2023. Velocities between image pairs are derived by the application of the autonomous Repeat Image Feature Tracking algorithm developed by Gardner et al.⁸².

Data availability

All data from this study is accessible free of charge in the ZENODO database under: https://doi.org/10.5281/zenodo.15673781.

Code availability

Pertinent code for the ice thickness reconstruction is available from GitHub at https://github.com/FAU-glacier-systems/ElmerIce_Thickness_ Reconstruction. Pertinent code for the buoyancy driven retreat model is available from GitHub at https://github.com/FAU-glacier-systems/Bouyancy_Glacier_Retreat.

Received: 4 September 2024; Accepted: 24 June 2025; Published online: 07 August 2025

References

- Zemp, M. et al. Global glacier mass changes and their contributions to sea-level rise from 1961 to 2016. Nature 568, 382–386 (2019).
- Marzeion, B., Kaser, G., Maussion, F. & Champollion, N. Limited influence of climate change mitigation on short-term glacier mass loss. *Nat. Clim. Change* 8, 305–308 (2018).
- Hugonnet, R. et al. Accelerated global glacier mass loss in the early twenty-first century. *Nature* 592, 726–731 (2021).

- 4. Braun, M. H. et al. Constraining glacier elevation and mass changes in South America. *Nat. Clim. Change* **9**. 130–136 (2019).
- Minowa, M., Skvarca, P. & Fujita, K. Climate and surface mass balance at Glaciar Perito Moreno, Southern Patagonia. *J. Clim.* 36, 625–641 (2023).
- Aniya, M. Recent glacier variations of the Hielos Patagónicos, South America, and their contribution to sea-level change. Arct., Antarct., Alp. Res. 31, 165–173 (1999).
- Schaefer, M., Machguth, H., Falvey, M., Casassa, G. & Rignot, E. Quantifying mass balance processes on the Southern Patagonia Icefield. *Cryosphere* 9, 25–35 (2015).
- Sakakibara, D. & Sugiyama, S. Ice-front variations and speed changes of calving glaciers in the Southern Patagonia Icefield from 1984 to 2011. JGR Earth Surf. 119, 2541–2554 (2014).
- Abdel Jaber, W., Rott, H., Floricioiu, D., Wuite, J. & Miranda, N. Heterogeneous spatial and temporal pattern of surface elevation change and mass balance of the Patagonian ice fields between 2000 and 2016. Cryosphere 13, 2511–2535 (2019).
- Minowa, M., Schaefer, M., Sugiyama, S., Sakakibara, D. & Skvarca, P. Frontal ablation and mass loss of the Patagonian icefields. *Earth Planet. Sci. Lett.* 561, 116811 (2021).
- Malz, P. et al. Elevation and mass changes of the Southern Patagonia Icefield Derived from TanDEM-X and SRTM Data. *Remote Sens.* 10, 188 (2018).
- Minowa, M., Schaefer, M. & Skvarca, P. Effects of topography on dynamics and mass loss of lake-terminating glaciers in southern Patagonia. J. Glaciol. 1–18 https://doi.org/10.1017/jog.2023.42 (2023).
- Sakakibara, D., Sugiyama, S., Sawagaki, T., Marinsek, S. & Skvarca, P. Rapid retreat, acceleration and thinning of Glaciar Upsala, Southern Patagonia Icefield, initiated in 2008. Ann. Glaciol. 54, 131–138 (2013).
- Secretaría de Turismo de la Municipalidad de El Calafate. https:// www.elcalafate.tur.ar/statistics.htm (2024).
- Zipfel, A. G. & Vanselow, K. A. El Chaltén, Argentine Patagonia: A Successful Combination of Conservation and Tourism? in Socio-Environmental Research in Latin America (ed. López, S.) 191–216 (Springer International Publishing, Cham, 2023). https://doi.org/10. 1007/978-3-031-22680-9 9.
- Minowa, M., Sugiyama, S., Sakakibara, D. & Sawagaki, T. Contrasting glacier variations of Glaciar Perito Moreno and Glaciar Ameghino, Southern Patagonia Icefield. Ann. Glaciol. 56, 26–32 (2015).
- McDonnell, M., Rupper, S. & Forster, R. Quantifying geodetic mass balance of the Northern and Southern Patagonian icefields since 1976. Front. Earth Sci. 10, 813574 (2022).
- Minowa, M., Sugiyama, S., Sakakibara, D. & Skvarca, P. Seasonal variations in ice-front position controlled by frontal ablation at Glaciar Perito Moreno, the Southern Patagonia Icefield. Front. Earth Sci. 5, (2017).
- Davies, B. J. & Glasser, N. F. Accelerating shrinkage of Patagonian glaciers from the Little Ice Age (~AD 1870) to 2011. *J. Glaciol.* 58, 1063–1084 (2012).
- Stuefer, M., Rott, H., Skvarca, P. & Glaciar, P. erito Moreno, Patagonia: climate sensitivities and glacier characteristics preceding the 2003/04 and 2005/06 damming events. J. Glaciol. 53, 3–16 (2007).
- Benn, D. I., Warren, C. R. & Mottram, R. H. Calving processes and the dynamics of calving glaciers. *Earth-Sci. Rev.* 82, 143–179 (2007).
- 22. Truffer, M. & Motyka, R. J. Where glaciers meet water: Subaqueous melt and its relevance to glaciers in various settings. *Rev. Geophys.* **54**, 220–239 (2016).
- Enderlin, E. M., Howat, I. M. & Vieli, A. High sensitivity of tidewater outlet glacier dynamics to shape. *Cryosphere* 7, 1007–1015 (2013).
- Robel, A. A., Pegler, S. S., Catania, G., Felikson, D. & Simkins, L. M. Ambiguous stability of glaciers at bed peaks. *J. Glaciol.* 68, 1177–1184 (2022).

- Sugiyama, S. et al. Ice speed of a calving glacier modulated by small fluctuations in basal water pressure. Nat. Geosci. 4, 597–600 (2011).
- Zekollari, H., Huss, M., Farinotti, D. & Lhermitte, S. Ice-dynamical glacier evolution modeling—a review. Rev. Geophys. 60, e2021RG000754 (2022).
- 27. Schmidt, L. S. et al. Dynamic simulations of Vatnajökull ice cap from 1980 to 2300. *J. Glaciol.* **66**, 97–112 (2020).
- 28. Jouvet, G., Huss, M., Funk, M. & Blatter, H. Modelling the retreat of Grosser Aletschgletscher, Switzerland, in a changing climate. *J. Glaciol.* **57**, 1033–1045 (2011).
- Gantayat, P., Kulkarni, A. V., Srinivasan, J. & Schmeits, M. J. Numerical modelling of past retreat and future evolution of Chhota Shigri glacier in Western Indian Himalaya. *Ann. Glaciol.* 58, 136–144 (2017).
- Zekollari, H., Fürst, J. J. & Huybrechts, P. Modelling the evolution of Vadret da Morteratsch, Switzerland, since the Little Ice Age and into the future. J. Glaciol. 60, 1155–1168 (2014).
- Fürst, J. J. et al. The foundations of the Patagonian icefields. Commun. Earth Environ. 5, 142 (2024).
- 32. Fürst, J. J. et al. The ice-free topography of Svalbard. *Geophys. Res. Lett.* **45**, 11,760–11,769 (2018).
- 33. Krieger, G. et al. TanDEM-X: A radar interferometer with two formation-flying satellites. *Acta Astronautica* **89**, 83–98 (2013).
- 34. Farr, T. G. et al. The Shuttle Radar Topography Mission. *Rev. Geophys.* **45**, RG2004 (2007).
- Gardner, A., Fahnestock, M. & Scambos, T. MEASURES ITS_LIVE Regional Glacier and Ice Sheet Surface Velocities, Version 1. NASA Natl. Snow Ice Data Cent. Distrib. Act. Arch. Cent. https://doi.org/10. 5067/6II6VW8LLWJ7 (2022).
- Sugiyama, S. et al. Thermal structure of proglacial lakes in Patagonia. JGR Earth Surf. 121, 2270–2286 (2016).
- Sugiyama, S. et al. Subglacial discharge controls seasonal variations in the thermal structure of a glacial lake in Patagonia. *Nat. Commun.* 12, 6301 (2021).
- Berthier, E., Arnaud, Y., Vincent, C. & Rémy, F. Biases of SRTM in high-mountain areas: Implications for the monitoring of glacier volume changes. *Geophys. Res. Lett.* 33, 2006GL025862 (2006).
- Agosta, E. A., Hurtado, S. I. & Martin, P. B. "Easterlies"-induced precipitation in eastern Patagonia: Seasonal influences of ENSO'S FLAVOURS and SAM. Int. J. Climatol. 40, 5464–5484 (2020).
- Bondzio, J. H. et al. The mechanisms behind Jakobshavn Isbræ's acceleration and mass loss: A 3-D thermomechanical model study. *Geophys. Res. Lett.* 44, 6252–6260 (2017).
- Bown, F. et al. Recent ice dynamics and mass balance of Jorge Montt Glacier, Southern Patagonia Icefield. J. Glaciol. 65, 732–744 (2019).
- 42. Naruse, R., Skvarca, P. & Takeuchi, Y. Thinning and retreat of Glaciar Upsala, and an estimate of annual ablation changes in southern Patagonia. *Ann. Glaciol.* **24**, 38–42 (1997).
- Batchelor, C. L. et al. Rapid, buoyancy-driven ice-sheet retreat of hundreds of metres per day. *Nature* 617, 105–110 (2023).
- 44. Lopez, P. et al. A regional view of fluctuations in glacier length in southern South America. *Glob. Planet. Change* **71**, 85–108 (2010).
- 45. Sugiyama, S., Minowa, M. & Schaefer, M. Underwater ice terrace observed at the front of Glaciar Grey, a freshwater calving glacier in Patagonia. *Geophys. Res. Lett.* **46**, 2602–2609 (2019).
- De Angelis, H. Hypsometry and sensitivity of the mass balance to changes in equilibrium-line altitude: the case of the Southern Patagonia Icefield. J. Glaciol. 60, 14–28 (2014).
- Bannwart, J. et al. Elevation bias due to penetration of spaceborne radar signal on Grosser Aletschgletscher, Switzerland. *J. Glaciol*. 1–40 https://doi.org/10.1017/jog.2024.37 (2024).
- Dussaillant, I., Berthier, E. & Brun, F. Geodetic mass balance of the Northern Patagonian Icefield from 2000 to 2012 using two independent methods. Front. Earth Sci. 6, 8 (2018).

- Lapazaran, J. J., Otero, J., Martín-Español, A. & Navarro, F. J. On the errors involved in ice-thickness estimates I: ground-penetrating radar measurement errors. *J. Glaciol.* 62. 1008–1020 (2016).
- Trevers, M., Payne, A. J., Cornford, S. L. & Moon, T. Buoyant forces promote tidewater glacier iceberg calving through large basal stress concentrations. *Cryosphere* 13, 1877–1887 (2019).
- Collazo, S. et al. Influence of large-scale circulation and local feedbacks on extreme summer heat in Argentina in 2022/23. Commun. Earth Environ. 5, 231 (2024).
- Huss, M., Jouvet, G., Farinotti, D. & Bauder, A. Future high-mountain hydrology: a new parameterization of glacier retreat. *Hydrol. Earth Syst. Sci.* https://doi.org/10.5194/hess-14-815-2010 (2010).
- Trüssel, B. L., Motyka, R. J., Truffer, M. & Larsen, C. F. Rapid thinning of lake-calving Yakutat Glacier and the collapse of the Yakutat Icefield, southeast Alaska, USA. J. Glaciol. 59, 149–161 (2013).
- Trüssel, B. L. et al. Runaway thinning of the low-elevation Yakutat Glacier, Alaska, and its sensitivity to climate change. *J. Glaciol.* 61, 65–75 (2015).
- Hock, R. A distributed temperature-index ice- and snowmelt model including potential direct solar radiation. *J. Glaciol.* 45, 101–111 (1999)
- Sauter, T. Revisiting extreme precipitation amounts over southern South America and implications for the Patagonian Icefields. *Hydrol. Earth Syst. Sci.* 24, 2003–2016 (2020).
- Bravo, C., Bozkurt, D., Ross, A. N. & Quincey, D. J. Projected increases in surface melt and ice loss for the Northern and Southern Patagonian Icefields. Sci. Rep. 11, 16847 (2021).
- Schaefer, M., Machguth, H., Falvey, M. & Casassa, G. Modeling past and future surface mass balance of the Northern Patagonia Icefield. *JGR Earth Surf.* 118, 571–588 (2013).
- Lenaerts, J. T. M. et al. Extreme precipitation and climate gradients in Patagonia revealed by high-resolution regional atmospheric climate modeling. J. Clim. 27, 4607–4621 (2014).
- Mernild, S. H., Liston, G. E., Hiemstra, C. & Wilson, R. The Andes Cordillera. Part III: glacier surface mass balance and contribution to sea level rise (1979–2014). *Int. J. Climatol.* 37, 3154–3174 (2017).
- Rignot, E., Rivera, A. & Casassa, G. Contribution of the Patagonia icefields of South America to sea level rise. Science 302, 434–437 (2003).
- 62. Weidemann, S. S. et al. Glacier mass changes of lake-terminating grey and tyndall glaciers at the Southern Patagonia icefield derived from geodetic observations and energy and mass balance modeling. *Front. Earth Sci.* **6**, 81 (2018).
- Fürst, J. J. et al. Application of a two-step approach for mapping ice thickness to various glacier types on Svalbard. *Cryosphere* 11, 2003–2032 (2017).
- Turton, J. V., Kirchgaessner, A., Ross, A. N., King, J. C. & Kuipers Munneke, P. The influence of föhn winds on annual and seasonal surface melt on the Larsen C Ice Shelf, Antarctica. *Cryosphere* 14, 4165–4180 (2020).
- Bannister, D. & King, J. C. The characteristics and temporal variability of föhn winds at King Edward Point, South Georgia. *Int. J. Climatol.* 40, 2778–2794 (2020).
- Frank, T. et al. Geometric controls of tidewater glacier dynamics. Cryosphere 16, 581–601 (2022).
- Lodolo, E. The submerged footprint of Perito Moreno glacier. Sci. Rep. https://doi.org/10.1038/s41598-020-73410-8 (2020).
- Blindow, N., Salat, C., Gundelach, V., Buschmann, U. & Kahnt, W. Performance and calibration of the helicoper GPR system BGR-P30. in 2011 6th International Workshop on Advanced Ground Penetrating Radar (IWAGPR) 1–5 (IEEE, Aachen, Germany, 2011). https://doi.org/ 10.1109/IWAGPR.2011.5963896.
- Sommer, C., Fürst, J. J., Huss, M. & Braun, M. H. Constraining regional glacier reconstructions using past ice thickness of deglaciating areas

- a case study in the European Alps. *Cryosphere* **17**, 2285–2303 (2023).
- Millan, R. et al. Ice Thickness and Bed Elevation of the Northern and Southern Patagonian Icefields. *Geophys. Res. Lett.* 46, 6626–6635 (2019).
- RGI Consortium. Randolph Glacier Inventory A Dataset of Global Glacier Outlines, Version 6. National Snow and Ice Data Center https://doi.org/10.7265/4M1F-GD79 (2017).
- Kalnay, E. et al. The NCEP/NCAR 40-Year Reanalysis Project. Bull. Am. Meteor. Soc. 77, 437–471 (1996).
- Mouginot, J. & Rignot, E. Ice motion of the Patagonian Icefields of South America: 1984–2014. *Geophys. Res. Lett.* 42, 1441–1449 (2015).
- Linsbauer, A., Paul, F. & Haeberli, W. Modeling glacier thickness distribution and bed topography over entire mountain ranges with GlabTop: Application of a fast and robust approach. *J. Geophys. Res.* 117, 2011JF002313 (2012).
- Hindmarsh, R. C. A. The role of membrane-like stresses in determining the stability and sensitivity of the Antarctic ice sheets: back pressure and grounding line motion. *Philos. Trans. R. Soc. A.* 364, 1733–1767 (2006).
- Zink, M. et al. TanDEM-X mission status: The complete new topography of the Earth. in 2016 IEEE International Geoscience and Remote Sensing Symposium (IGARSS) 317–320 (IEEE, Beijing, 2016). https://doi.org/10.1109/IGARSS.2016.7729075.
- Nuth, C. & Kääb, A. Co-registration and bias corrections of satellite elevation data sets for quantifying glacier thickness change. Cryosphere 5, 271–290 (2011).
- RGI Consortium. Randolph Glacier Inventory A Dataset of Global Glacier Outlines, Version 7. NASA National Snow and Ice Data Center Distributed Active Archive Center https://doi.org/10.5067/ F6JMOVY5NAVZ (2023).
- Rolstad, C., Haug, T. & Denby, B. Spatially integrated geodetic glacier mass balance and its uncertainty based on geostatistical analysis: application to the western Svartisen ice cap. *Nor. J. Glaciol.* 55, 666–680 (2009).
- 80. Martone, M., Rizzoli, P. & Krieger, G. Volume Decorrelation Effects in TanDEM-X Interferometric SAR Data. *IEEE Geosci. Remote Sens. Lett.* **13**, 1812–1816 (2016).
- Rizzoli, P. et al. On the Derivation of Volume Decorrelation From TanDEM-X Bistatic Coherence. *IEEE J. Sel. Top. Appl. Earth Obs. Remote Sens.* 15, 3504–3518 (2022).
- Gardner, A. S. et al. Increased West Antarctic and unchanged East Antarctic ice discharge over the last 7 years. *Cryosphere* 12, 521–547 (2018).

Acknowledgements

M.K. was funded by the Deutsche Forschungsgemeinschaft via the grant DFG BR 2105/29-1/FU 1032/12-1. M.K. is an affiliated doctoral candidate at the international doctorate programme "Measuring and Modelling Mountain glaciers and ice caps in a Changing ClimAte (M3OCCA), funded by the Elite Network of Bavaria, Germany. J.J.F. received primary funding from the European Union's Horizon 2020 research and innovation programme via the European Research Council (ERC) as a Starting Grant (FRAGILE project) under grant agreement No 948290. The authors would also like to gratefully acknowledge the scientific support and HPC resources provided by the Erlangen National High Performance Computing Centre (NHR@FAU) of the Friedrich-Alexander-Universität Erlangen-Nürnberg (FAU). NHR funding is provided by federal and Bavarian state authorities. NHR@FAU hardware is partially funded by the German Research Foundation (DFG) - 440719683. We would like to thank the authorities and park rangers from the Parque Nacional Los Glaciares for supporting our field activities throughout our campaigns and for the productive collaboration. We also thank Masahiro Minowa for lending out his transducer for our bathymetric survey. Special

thanks to Steffen Welsch for great support in field activities. The TanDEM-X data were kindly provided free of charge by the German Aerospace Centre (DLR) under AO mabra_XTI_GLAC0264.

Author contributions

M.K. joined the GPR acquisition and performed the GPR data analysis, ice thickness reconstruction, and developed the retreat model. He compiled all the figures and wrote the manuscript. C.S. processed the TanDEM-X elevation changes. N.B. developed the GPR system, supervised the GPR data acquisition and analysis. P.S. planned and organized the bathymetry survey, and contributed with L.R. to the interpretation and discussion of data. K.L. processed the bathymetric data. J.L.B.B. & P.R. coordinated new TanDEM-X data takes. J.J.F., M.H.B., N.B., P.S. and M.K. were part of the GPR field team. J.J.F. supervised the ice thickness reconstruction as well as the modelling. M.H.B. initiated and led the study, coordinated the field surveys. All authors revised the manuscript.

Funding

Open Access funding enabled and organized by Projekt DEAL.

Competing interests

The authors declare no competing interests.

Additional information

Supplementary information The online version contains supplementary material available at https://doi.org/10.1038/s43247-025-02515-7.

Correspondence and requests for materials should be addressed to Moritz Koch

Peer review information: Communications Earth and Environment thanks Ryan Wilson, Camilo Rada, and the other anonymous reviewer(s) for their contribution to the peer review of this work. Primary Handling Editors: Shin Sugiyama and Alireza Bahadori. A peer review file is available.

Reprints and permissions information is available at http://www.nature.com/reprints

Publisher's note Springer Nature remains neutral with regard to jurisdictional claims in published maps and institutional affiliations.

Open Access This article is licensed under a Creative Commons Attribution 4.0 International License, which permits use, sharing, adaptation, distribution and reproduction in any medium or format, as long as you give appropriate credit to the original author(s) and the source, provide a link to the Creative Commons licence, and indicate if changes were made. The images or other third party material in this article are included in the article's Creative Commons licence, unless indicated otherwise in a credit line to the material. If material is not included in the article's Creative Commons licence and your intended use is not permitted by statutory regulation or exceeds the permitted use, you will need to obtain permission directly from the copyright holder. To view a copy of this licence, visit http://creativecommons.org/licenses/by/4.0/.

© The Author(s) 2025